Real-time pedestal optimization and ELM control with 3D fields and gas flows on DIII-D

F.M. Laggner[1,2] ⓘ, D. Eldon[3] ⓘ, A.O. Nelson[1] ⓘ, C. Paz-Soldan[3] ⓘ, A. Bortolon[1] ⓘ, T.E. Evans[3] ⓘ, M.E. Fenstermacher[4], B.A. Grierson[1] ⓘ, Q. Hu[1] ⓘ, D.A. Humphreys[3] ⓘ, A.W. Hyatt[3], R. Nazikian[1] ⓘ, O. Meneghini[3] ⓘ, P.B. Snyder[3] ⓘ, E.A. Unterberg[5] ⓘ, E. Kolemen[2] ⓘ and the DIII-D team

[1] Princeton Plasma Physics Laboratory, Princeton, NJ 08543, United States of America
[2] Princeton University, Princeton, NJ 08544, United States of America
[3] General Atomics, San Diego, CA 92186, United States of America
[4] Lawrence Livermore National Laboratory, Livermore, CA 94550, United States of America
[5] Oak Ridge National Laboratory, Oak Ridge, TN 37831, United States of America

E-mail: flaggner@pppl.gov and ekolemen@princeton.edu

Abstract

The capabilities of the DIII-D tokamak's plasma control system (PCS) were expanded to allow for pedestal optimization and edge localized mode (ELM) control. Three proof of principle control schemes are presented that were successfully implemented and tested. These use multiple inputs from real-time (RT) diagnostics like a D_α based ELM monitor and edge profile measurements from Thomson scattering (TS) as well as 3D, i.e. non-axisymmetric, magnetic fields and gas puffs as actuators to regulate the density pedestal.

The first scheme targets to optimize the access of ELM suppression induced by non-axisymmetric magnetic perturbations (MPs). The conducted set of experiments identifies a path dependence of plasma confinement on the applied MP amplitude. The controller aims to transition into ELM suppression at the minimum 3D field amplitude and reduces it further afterwards, allowing for partial confinement recovery. Another pedestal control scheme is deployed to compensate the density 'pump-out' in MP ELM suppression by regulating the gas puff. This uses RT TS diagnostic data, extracting the pedestal height from the electron density (n_e) profiles and enables studies of the transition into and out of MP ELM suppression at constant density. A limit cycle behavior of edge rotation and MP amplitude persists under these conditions. The third control scheme combines MPs and gas puffs as actuators to perform pedestal density trajectory control to access Super high confinement mode (H-mode) and furthermore, allowing the integration of a radiative divertor in this regime. While MPs mainly impact the pedestal top density, the control scheme allows to loosen the tight coupling of pedestal top and separatrix density evolution.

With respect to ITER, the achieved results emphasize the need for an advanced control system to keep MP amplitude close to but above the ELM suppression threshold at all times, enabling high confinement and, respectively, at high fusion energy gain factor (Q). Furthermore, pedestal control enables detailed physics studies in present-day tokamaks and allows the exploration of core-edge integrated plasma scenarios.

Keywords: tokamak, super H-mode, edge localized modes, 3D fields

(Some figures may appear in colour only in the online journal)

Table 1. Overview of the implemented control schemes, the utilized sensors and actuators.

Controller	Purpose	Sensors	Actuators	Section
Optimized MP ELM suppression	Control 3D field amplitude minimization sustaining ELM suppression	D_α line radiation (D_α) ELM monitor	MP coil currents	3.2
n_e pedestal maximization	Compensation of density 'pump-out' in ELM suppression	RT Thomson scattering (TS) or laser interferometry (LI)	Gas fluxes	3.3
Integrated n_e pedestal regulation	Controlling the n_e pedestal evolution in Super H-mode	RT TS or LI	MP coil currents and gas fluxes	4

1. Introduction

The high confinement mode (H-mode) regime of tokamak operation offers attractive potential for fusion energy. However, the strong edge transport barrier in this regime is punctuated by edge localized modes (ELMs) [1], expelling particles and energy towards the divertor and first-wall. The expected ELM associated heat flux in ITER will exceed material limits [2] and therefore, necessitates ELM control for divertor protection [3, 4]. A promising candidate to actively suppress ELMs are non-axisymmetric 3D magnetic fields applied by in-vessel magnetic perturbation (MP) coils. MP ELM suppression was achieved in various machines like DIII-D [5], KSTAR [6], EAST [7] and AUG [8]. While understanding the underlying mechanisms leading to MP ELM suppression is a field of ongoing research [9–12], it was decided to equip ITER with a set of MP coils for ELM control [13–15]. ELM suppression usually comes together with a density 'pump-out' [16], i.e. a reduction of the pedestal density, which is also linked to a degradation of the plasma confinement arising from the same spectral components of the applied 3D field [17]. Such behavior is unfavorable when optimizing for maximum fusion performance. Nevertheless, it was reported that global confinement can recover, once the discharge transited into ELM suppression [18]. This indicates that there is some headroom for optimization of plasma performance while sustaining MP ELM suppression, which motivates advanced plasma control schemes to stay in this optimal regime of operation. Furthermore, future devices such as ITER will have long pulse operation, and simple feed-forward programming of MP coil currents is no longer suitable since the plasma and wall conditions may evolve and the 3D field amplitude would need to be adjusted correspondingly. Otherwise, ELM suppression might be lost at some point of the discharge as seen e.g. on KSTAR, which demonstrated MP ELM suppression for more than 30 s [19].

Multi-actuator pedestal electron density (n_e) control, which uses gas puff as well as 3D fields by MP coils, can be utilized to access and to sustain the Super H-mode regime. So far Super H-mode [20] has been achieved on DIII-D [21] and Alcator C-Mod [22]. It is a theoretically predicted high pedestal pressure regime [23], which would favorably scale to high fusion performance [24]. As key access conditions, high plasma shaping, which opens up the Super H-mode access, and significant heating power to achieve high edge temperatures, are required.

Furthermore, a distinct trajectory of the density has to be followed to establish low pedestal top collisionality at high density, leading to high pedestal pressure. Since the access and sustainment of Super H-mode crucially depends on the pedestal density [23], pedestal n_e control is in particular required when moving towards reactor relevant divertor conditions and scaling Super H-mode towards burning plasma devices [21].

In most present-day tokamaks, the typical discharge duration is shorter than the wall source equilibration time. Furthermore, gas puffs are typically used as the main actuator for density control. Under these conditions, the lowest achievable n_e is given by a 'natural' limit at zero gas puff, where plasma fueling just occurs from residual recycling gas in the machine. 3D fields and the corresponding density 'pump-out' represent a strong actuator with fast response that allows to decrease the pedestal density. A pedestal n_e control scheme, using both actuators, gas puff as well as 3D fields, expands the range of accessible n_e targets.

To support the design and identify the requirements for a ELM control system, present-day fusion facilities need to advance control development [25]. With this aim, real-time (RT) pedestal and ELM control schemes were implemented in the plasma control system (PCS) of DIII-D, which has been continuously evolved and upgraded over several decades of DIII-D operations [26, 27]. Table 1 provides an overview of the n_e control schemes with the utilized sensors and actuators that are introduced within this contribution.

The following work presents recently added capabilities of the DIII-D PCS (section 2) and the setup and application of ELM suppression optimization controller as well as a pedestal density controller. In section 3 the general idea of ELM suppression control is outlined, a schematic overview of the controller's capabilities is given (section 3.1) and two kinds of pedestal optimization in ELM suppression are presented (section 3.2, 3.3). Further, the finding of a path dependence to ELM suppression, a so-called hysteresis, is discussed, stressing that optimization of the applied 3D MP field and respectively the pedestal in ELM suppressed regimes is crucial for maximum plasma performance. Section 4 presents an multi-actuator pedestal density controller, which uses gas puff as well as 3D fields by MP coils to regulate the n_e pedestal. This controller is applied in experiments (section 4.3) to ensure constant pedestal density, while performing a feed-forward gas scan to move towards radiative divertor conditions. The prospects of the presented findings with regards to ITER are discussed in
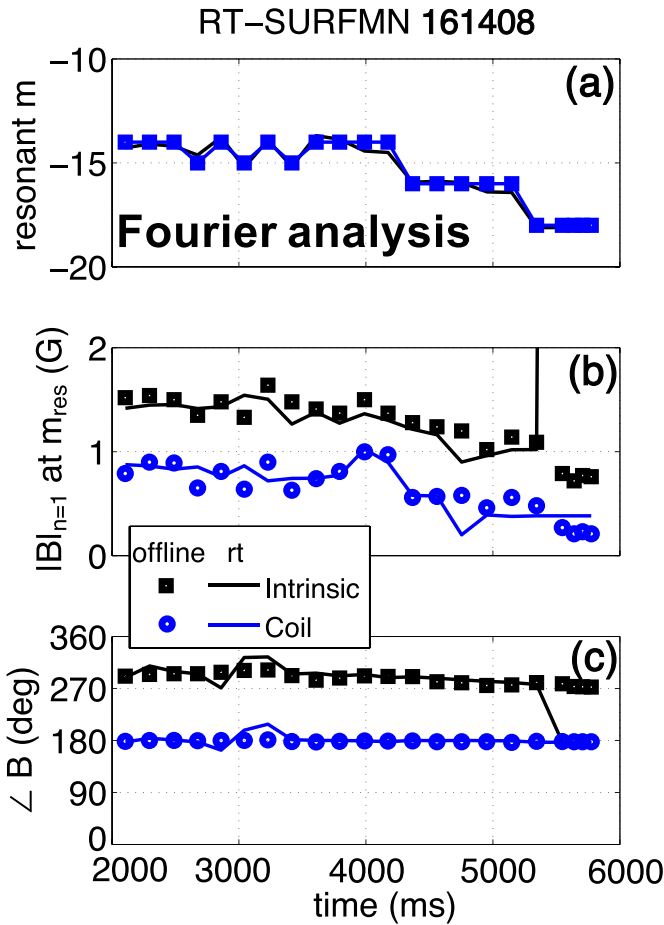
Figure 1. Real-time (RT) SURFMN benchmark: Comparison of RT calculations (solid lines) and offline analysis (symbols) for the intrinsic error field (black) and applied field (blue) (*a*) edge resonant harmonic poloidal mode number (m), (*b*) amplitude and (*c*) perturbation phase. The RT and offline calculations agree well throughout a plasma discharge with a shaping variation from upper single null (USN) to lower single null (LSN).

section 5, underlining the necessity of ELM suppression control in order to achieve high plasma performance. The contribution concludes with summary (section 6) and outlook (section 7), which emphasize the need to develop and advance edge and pedestal control further, ensuring high pedestal performance without harmful ELMs.

2. Sensors and RT models added to the DIII-D PCS

The DIII-D PCS undergoes a continuous evolution and expansion of capabilities mainly motivated by physics studies and potential control concepts for future devices. It provides an ideal test bed for developing new control schemes being well interfaced with various sensors and actuators. In context of the presented work, several extensions were added to the PCS, enhancing its capabilities towards RT pedestal profile characterization, ELM detection and RT calculation of the vacuum response of externally applied 3D fields. This addition of sensors and models enables advancement in possible control schemes for MP ELM suppression and pedestal n_e control.
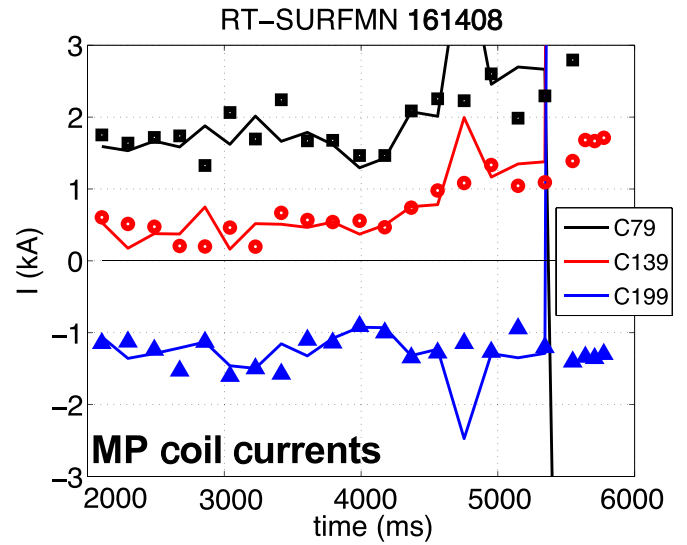

Figure 2. C-coil currents for RT error field correction (EFC): Calculated in RT (solid lines) and offline (symbols) for different coils of the C-coil set (black, red and blue).

On the sensor side of the PCS capabilities, the RT Thomson scattering (TS) diagnostic [28–30] was extended by a pedestal RT fitting algorithm for the n_e and electron temperature (T_e) profiles. Here, a tanh function [31] with a polynomial modification in the core is fitted to the measured data. The fitted parameters from this profile representation, directly provide the pedestal height and width, which can serve as inputs to pedestal control schemes. Furthermore, the D_α line radiation (D_α) in the divertor is used as a RT sensor to detect the occurrence of ELMs [32], which appear as D_α spikes. At the transition into ELM suppression, D_α drops to its baseline level. Using these criteria, a RT ELM detection algorithm based on D_α measurements evaluates the ELM repetition frequency (f_{ELM}) [32] and the transition to ELM suppression.

RT-capable models are necessary to predict the system's response when actuators are applied. When using 3D fields as an actuator, a direct calculation of their effects on the plasma is useful to optimize the control scheme and gains. An initial step in this direction was taken by implementing a RT version of the SURFMN code [13] into the DIII-D PCS. The SURFMN code calculates the 3D perturbing fields on a given magnetic surface and decomposes them into constituent Fourier harmonics. This is *a priori* independent of the external coil set. For a given coil set, RT SURFMN calculates the vacuum edge pitch-resonant and kink-resonant harmonics of the applied 3D MP, induced island sizes, and the Chirikov parameter (σ_{chir}) [33]. The relationship between the vacuum and the plasma responses for specific plasma regimes can be approximated via off-line IPEC calculations [34] and loaded to the PCS system. A control scheme could then adjust the relative phase between upper and lower MP coil sets as the plasma boundary and safety factor (*q*) profile evolve. This enables optimization of the effectiveness of the MP field penetration based on theoretical predictions for ELM suppression [35, 36]. Another application of the RT plasma response calculation is error field correction (EFC). In contrast to MP ELM suppression applications where the
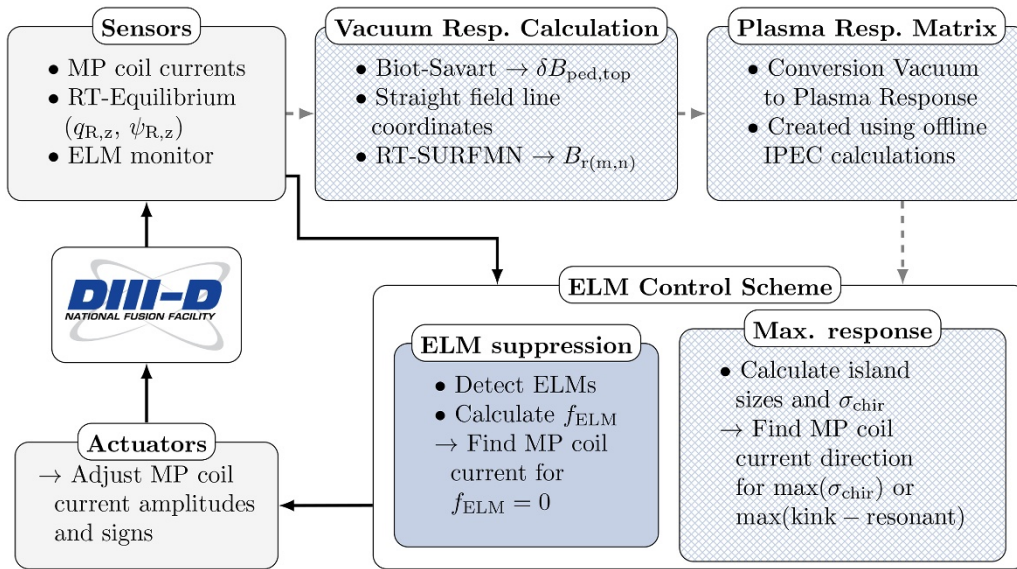
Figure 3. Schematic outline of the plasma control system (PCS) building blocks for ELM control: deployed (solid) and possible future (dashed) RT control loops on DIII-D.

response is maximized, EFC aims to compensate the resonant field components of the intrinsic error field. A simple type of EFC is usually applied in almost every DIII-D discharge. An empirical model that is based on measurements of the intrinsic error fields [37, 38] is used to scale the applied compensating MP amplitude based on plasma current (I_p) and toroidal magnetic field (B_θ).

Using a RT version of SURFMN provides a more accurate description of the resonant field components. This procedure is shown to predict the optimal EFC configuration in amplitude and phase [17] for the internal I-coil and the external C-coil coil sets on DIII-D. The RT model was implemented and tested for $n = 1$ and $n = 2$ EFC for evolving plasma conditions, finding the same optimal MP coil currents as detailed offline analysis. Figure 1 presents a benchmark of the RT calculations (solid lines) against the offline analysis (symbols) of the intrinsic $n = 1$ error field (black) and the field provided by the external C-coils.

The RT calculation reproduces the edge resonant harmonic poloidal mode number (m), the perturbation amplitude for the C-coil and the phase angle from the offline calculations throughout a plasma discharge that scanned the shape from upper single null (USN) to lower single null (LSN), affecting as well the edge safety factor (q_{95}). Small differences between RT and offline analysis originate from the input equilibria, which are evaluated on different times, roughly ± 10 ms, and the RT equilibria have less convergence constraints. For exactly the same input equilibria RT and offline SURFMN would come to the same solution. Figure 2 shows the calculated currents (lines: RT calculation, symbols: offline analysis) that need to be applied to the individual coils (black, red and blue) to compensate the intrinsic error field.

3. Setup of an ELM suppression control scheme

The following section discusses the implementation of two control schemes that where deployed to optimize MP ELM suppression.

3.1. ELM suppression control setup

A schematic overview of the implemented PCS building blocks to achieve, sustain and optimize 3D field-induced ELM suppression is shown in figure 3.

Two options for control loops are indicated. While a more sophisticated loop that includes the response calculation via RT SURFMN and optimization of the maximum response is envisaged in the future, the initial implementation uses a simplified loop bypassing this calculation. For first ELM suppression experiments (section 3.2), the RT ELM monitor servers as input and the MP coil amplitude is applied in a fixed coil configuration and parity. The amplitude of the MP coil currents are adjusted accordingly to bring the plasma into a state of a preset f_{ELM} or to ELM suppression ($f_{\mathrm{ELM}} = 0$). Once the plasma transitions into ELM suppression, the applied MP coil currents are reduced to minimize the confinement degradation.

3.2. Experiments using the ELM control system

In a first step, the transition into ELM suppression was optimized in the sense that the applied MP coil currents were reduced after the transition into ELM suppression occurs. Time traces of this experiment are shown in figure 4.

Here, three plasma discharges are compared: DIII-D discharge 159 442 (black) is the ELMy reference case, while discharge 159 440 (red) and 159 443 (blue) show MP induced ELM suppression. The discharges were performed at B_θ 1.95 T and I_p 1.6 MA resulting in q_{95} of roughly 3.5. The internal MP coils (I-coils) were configured in $n = 3$ configuration with even parity of the upper and lower row. In both cases with applied MP, the controller was able to reduce the amplitude of the MP coil currents (figure 4(*e*)) towards a pre-programmed lower threshold. Here, this threshold was empirically determined in a reference plasma discharge using steps of the MP coil amplitude similar to the ones presented in figure 6. As an ELM occurs, the controller increases the MP coil amplitude as response to the potentially lost ELM suppression (blue).
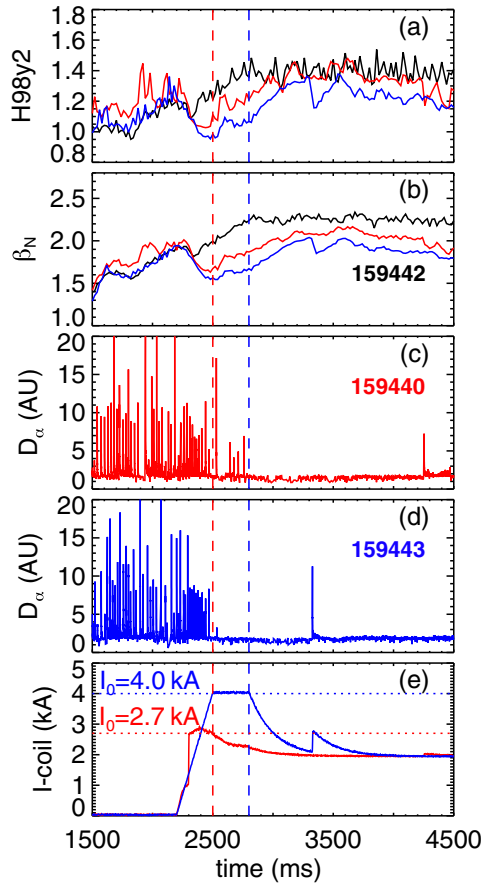
Figure 4. MP control enables ELM suppression with minimal confinement reduction: (*a*) confinement enhancement factor ($H_{98(y,2)}$), (*b*) normalized ratio of thermal to magnetic pressure (β_N), (*c*), (*d*) divertor D_α emission (ELM monitor) and (*e*) MP coil current for the ELMy reference (black), high initial MP coil current (blue, 4 kA) and reduced initial MP coil current (red, 2.7 kA). ELM suppression is achieved, however, lower confinement is observed throughout the remaining discharge, when a higher initial MP coil current is applied.

Figure 5. MP coil current reduction enables pedestal recovery while staying in ELM suppression: (*a*) MP coil current, (*b*) β_N, (*c*) divertor D_α emission (ELM monitor), (*d*) pedestal pressure (*P*) and (*e*) angular frequency of the perpendicular electron flow ($\omega_{\perp,e}$) profiles. The pedestal pressure and edge rotation can recover and β_N increases as the MP coil current is reduced up to the point where ELM suppression is lost.

The reduction of the applied MP (enabled at the dashed vertical lines) led to a partial recovery of the confinement enhancement factor ($H_{98(y,2)}$) and normalized ratio of thermal to magnetic pressure (β_N) (figure 4(*a*) and (*b*)). Even though the final MP coil currents of both ELM suppressed states are the same, the $H_{98(y,2)}$ and β_N recovery exhibits a path dependence. High initial MP coil currents led to lower recovery of confinement and performance later on in the discharge. This performance degradation effect likely comes with the excitation of core instabilities, which persist after reducing the initial MP amplitude.

Figure 5 presents the edge profiles of thermal pressure (*p*) and perpendicular electron flow ($\omega_{\perp,e}$) of discharge 159 443 (blue in figure 4) as the controller reduces the MP coil currents (top panel). Immediately after the transition into ELM suppression β_N is at its minimum and the *p* pedestal is relatively low though high $\omega_{\perp,e}$ exhibits strong rotation shear in the region of the depth of the radial electric field well ($\max(-E_r)$) (blue profiles). As the MP amplitude
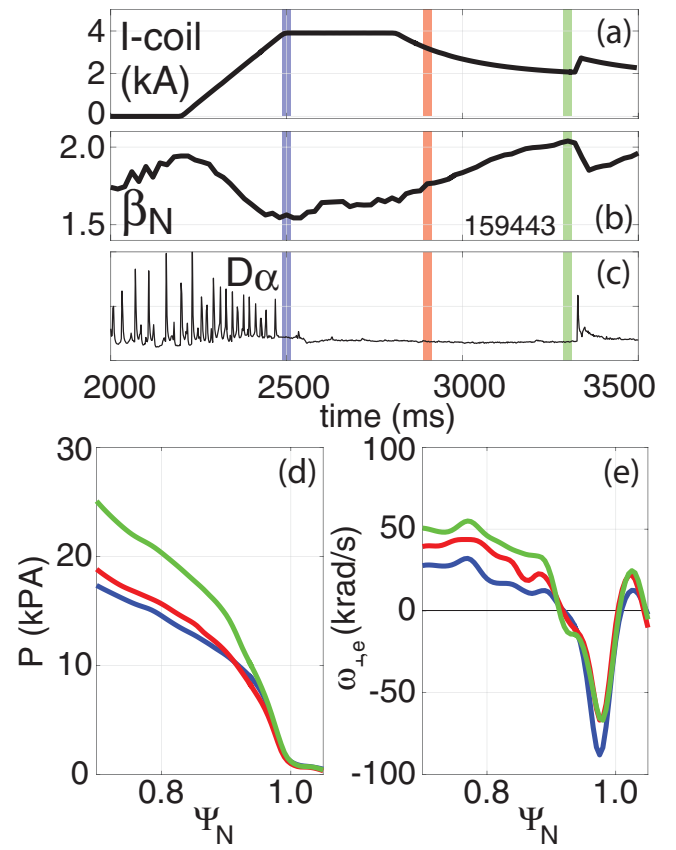
is reduced, first the pedestal top $\omega_{\perp,e}$ is enhanced (red), while the pedestal pressure recovers slowly, being accompanied by a slight increase of β_N. As the MP amplitude is reduced further, the pedestal top *p* increases and $\omega_{\perp,e}$ at the pedestal top continues to spin up (green). This happens just before a single ELM crash occurs (compare to figure 5(*c*)), where the pedestal has evolved up to a state which is likely close to the peeling-ballooning (PB) stability limit [39, 40] and therefore, ELMs become more likely to appear.

In summary, the presented experiments showed a path dependence, i.e. a hysteresis of the plasma confinement recovery: Even for the same final perturbing MP coil currents, starting with higher initial 3D field leads to lower recovery down the path. This control is motivated by the experimental result that the $H_{98(y,2)}$ decreases substantially with a MP coil current exceeding the required threshold for ELM suppression [41]. The proof of principle implementation at DIII-D highlights that the concept of optimized ELM suppression access is beneficial and feasible with MP coil feedback regulation.
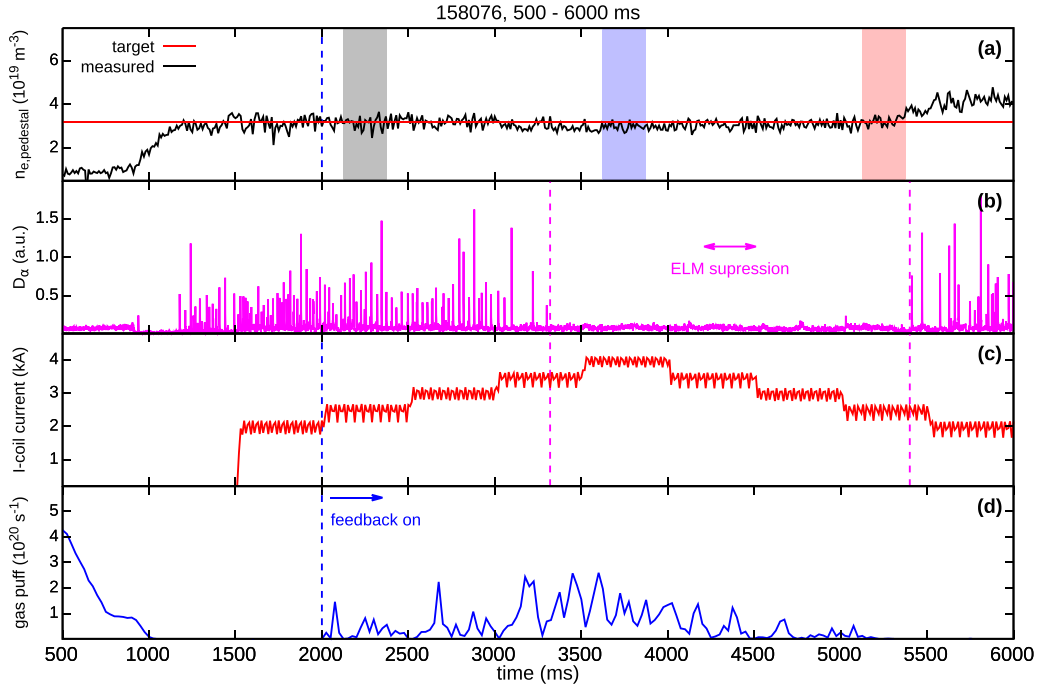
Figure 6. Hysteresis in accessing and exiting ELM suppression at controlled edge electron density (n_e): (*a*) pedestal n_e, (*b*) D_α line radiation (D_α), (*c*) MP coil current and (*d*) gas puff.

3.3. Establishment of an ELM suppressed, optimized pedestal

Feedback control using a pedestal RT TS n_e measurement and gas puff was utilized to regulate the pedestal n_e, when varying the MP coils currents. Typically, the 3D field amplitude is strongly correlated with the strength of density 'pump-out'. This means that higher applied 3D field amplitudes lead to a stronger reduction of n_e. To compensate for the density reduction during the MP application, additional gas can be puffed. Figure 6 presents a plasma discharge where the MP coil current was first stepped up and then down. The gas puff (figure 6(*d*)) was feedback controlled on a RT TS pedestal n_e measurement (figure 6(*a*)). As the MP coil current and correspondingly the 3D field amplitude is stepped up the gas puff rate increases to compensate the stronger density 'pump-out'. This indicates the possibility to at least partially compensate the density 'pump-out' and recover the pedestal degradation by additional fueling. Towards the highest applied MP coil current, the discharge transitions into a ELM suppressed state (see figure 6(*b*)). Because of the n_e feedback this results in minimal reduction of n_e. The slight change of the pedestal n_e in and out of ELM suppression indicates a near-threshold effect, which also depends on the applied MP coil amplitude. This goes in hand with the observation that a certain 3D field amplitude threshold is required to achieve ELM suppression [9]. As the MP coil current is stepped down during the remainder of the plasma discharge, ELM suppression can be sustained at lower 3D field amplitude, similar as already discussed in section 3.2.

The pedestal profiles in phases (compare to the colored areas in figure 6(*a*)) during ELMy H-mode (black), after transiting into ELM suppression (blue) and before the loss of ELM suppression (red) are presented in figure 7. As n_e is feedback controlled the pedestal top n_e (figure 7(*a*)) is only slightly reduced (blue) and towards the loss of ELM suppression the n_e profile (red) is similar to the one during ELMy H-mode. While the T_e profiles remain similar (figure 7(*b*)), the impurity density of fully stripped carbon ($n_{C^{6+}}$) (figure 7(*c*)) as well as impurity temperature of fully stripped carbon ($T_{C^{6+}}$) (figure 7(*d*)) increase throughout the discharge. A cyclic behavior of $\omega_{\perp,e}$ in the steep gradient region and towards the pedestal top is observed. While $\omega_{\perp,e}$ decreases significantly at the transition into ELM suppression, because the toroidal rotation increases, it evolves back to the structure of ELMy H-mode before the ELM suppression is lost. Similar behavior was recently reported from KSTAR [42] and it is consistent with the observation of a rotation threshold for ELM suppression [12].

Figure 8 illustrates the limit cycle behavior of MP field amplitude and edge toroidal rotation (v_{tor}) at the pedestal top. The color bar indicates the f_{ELM} ($f_{ELM} = 0$ prescribes ELM suppressed conditions). This hysteresis behavior for ELM suppression can be outlined as follows: Initially the 3D fields need to penetrate into the plasma, which requires a higher MP coil current. When transitioning in ELM suppression v_{tor} goes up (phase (*a*)), while $\omega_{\perp,e}$ is reduced in the pedestal region. The modification of the edge flows likely allows better coupling of the 3D field. Once in ELM suppression the 3D field amplitude can be reduced though remaining high v_{tor} (phase (*b*)). As the pedestal $n_{C^{6+}}$ and $T_{C^{6+}}$ increase, the pedestal pressure increases. This might push the pedestal structure towards its stability limit, which leads to ELMs, slow down of v_{tor} and loss of ELM suppression (phase (*c*)).

In summary, two edge control schemes were successfully implemented and applied to achieve and optimize ELM
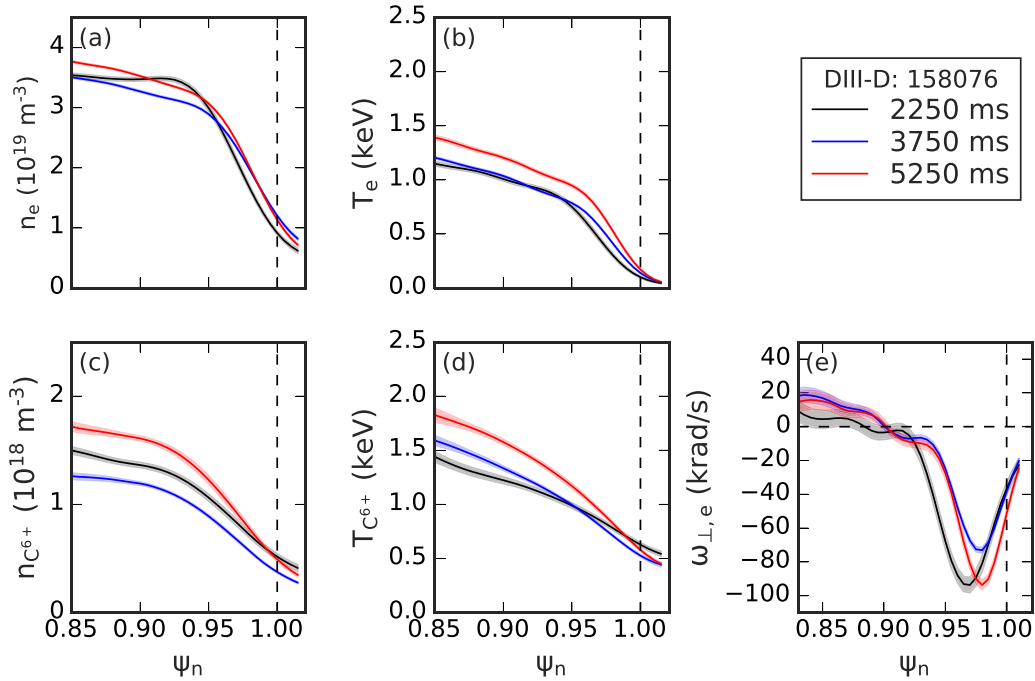
Figure 7. Edge profiles in ELM suppression: (*a*) n_e, (*b*) electron temperature (T_e), (*c*) impurity density of fully stripped carbon ($n_{C^{6+}}$), (*d*) impurity temperature of fully stripped carbon ($T_{C^{6+}}$) and (*e*) $\omega_{\perp,e}$ during ELMy H-mode (black), after transiting into ELM suppression (blue) and before the loss of ELM suppression (red). The considered intervals are also indicated in figure 6(*a*) by shaded areas in the corresponding colors. When transiting into ELM suppression, $\omega_{\perp,e}$ decreases strongly. As the 3D field amplitude is reduced, $\omega_{\perp,e}$ increases again.
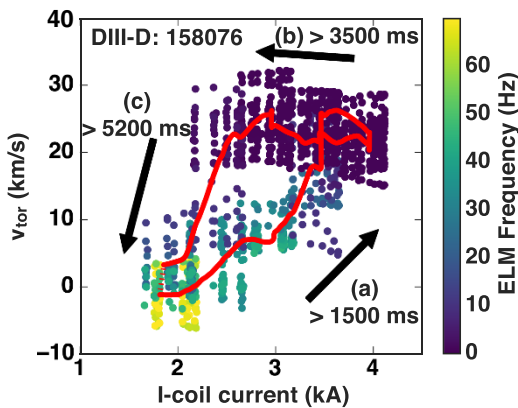

Figure 8. Limit cycle behavior of MP coil current and edge toroidal rotation (v_{tor}): The red path indicates the discharge evolution. In phase (*a*) the MP coil current is increased, edge rotation spins up and the ELM repetition frequency (f_{ELM}) vanishes. During phase (*b*) the 3D field amplitude is reduced, while the plasma remains spinning until ELM suppression is lost in phase (*c*).

suppressed pedestals. While a feedback controlled reduction of the MP coil current and correspondingly lowering of the 3D field amplitude can be used to achieve optimal pedestal performance, density feedback using gas puff can be utilized to partially compensate the density 'pump-out'. In the following both of these actuators, 3D fields and gas puff, are combined to construct an multi-actuator pedestal n_e control system.

4. Pedestal density control scheme

Typically, n_e is controlled using a line integrated n_e measurement from laser interferometry (LI) and gas valves as actuators [43–45]. Such schemes can become significantly more complex when recycling and pumping are taken into account using models [46] or even more complex when aiming for fully predictive profile control [47]. Towards ITER and future demonstration power plants, which also will have line integrated n_e measurements [48–50], the main actuator will become deuterium (D) and tritium (T) pellet injection systems [51].

The limitation of gas and pellet n_e control schemes is that the 'natural' n_e at zero actuator throughput represents a lower limit of the accessible control range. Moreover, these actuators provide in first order a radially fixed distribution that can only be varied in amplitude, fundamentally limiting the access of plasma conditions that are required to perform experimental studies. This motivated the implementation of a feedback controller that uses gas puff as well as 3D fields as actuators to regulate the pedestal density. Furthermore, the plasma response to MP fields is faster than to gas puff, allowing for a shorter lag between controller action and system response. Ultimately, the controller can be utilized to loosen the tight coupling between pedestal and separatrix density (section 4.2).

4.1. Setup of the pedestal density control loop

The implemented controller increases the gas flow when the n_e falls below the target value, while the MP coils can be used in
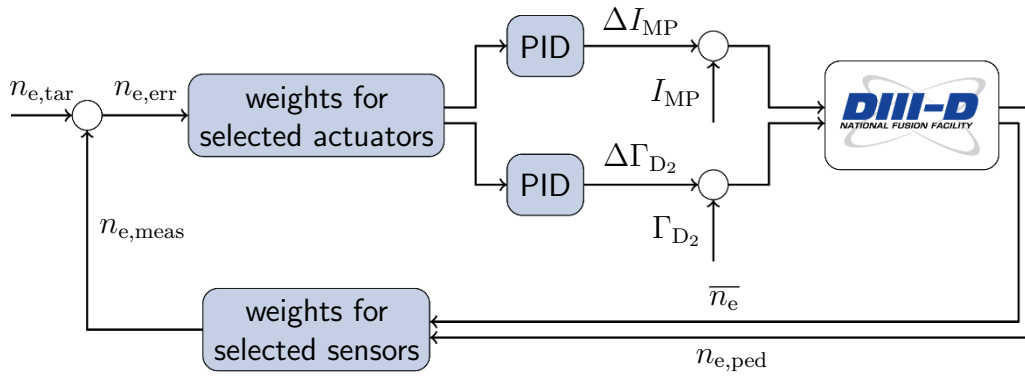
Figure 9. Schematic overview of the gas and 3D field pedestal density feedback loop.

a complementary way to control MP density 'pump-out' and actively lower n_e when above the target. A schematic overview is shown in figure 9. The feedback control loop features a variety of actuators including various gas valves available in DIII-D, as well as a scaling parameter for the MP coil current. The sensors are line integrated n_e measurements from LI and RT-TS channels, which can be individually selected or combined with different weights. A similar flexibility for selection and weighted combination is also implemented for the actuators. From the calculated error and the corresponding weights, standard proportional - integral - derivative (PID) controllers are used to adjust the selected actuators. The RT n_e diagnostics at DIII-D [28, 52] monitor the changes and are combined to the n_e measurement ($n_{e,meas}$), from which the error for the following iteration of the loop is calculated. This feedback loop is implemented in such a way that it allows other activated controllers to use the same actuators. The EFC controller, which also uses the MP coils as actuator, can be applied in parallel to the pedestal n_e control. Similarly, the pedestal n_e control can be performed simultaneously to feed-forward puffing from various gas valves at different locations around DIII-D. This enables to feedback control the pedestal n_e using the MP coils, while performing a feed-forward gas puff scan (section 4.3).

4.2. Multi-actuator density pedestal control

The introduced pedestal n_e feedback cycle was implemented in the DIII-D PCS and successfully tested. Figure 10 shows the application of the algorithm to regulate the line average density towards the end of a density ramp, which is induced by a L-H transition and further on to regulate the density during a phase of feed-forward gas puff. Here, MP coils in $n = 3$ configuration were used in an optimal configuration with odd coil parity. This aligns the perturbation to the intrinsic $n = 3$ error field and leads to a strong plasma response that is accompanied by a strong density 'pump-out'. After a short initialization period, the feedback loop is turned on and the MP coil currents (see figure 10(c)) are regulated using the MP coil current multiplier (see figure 10(b)). As the density approaches the target, the MP coil current multiplier is reduced and additional gas is introduced on top of the feed-forward gas puff. In the presented case an offset is added to the gas feedback error to avoid
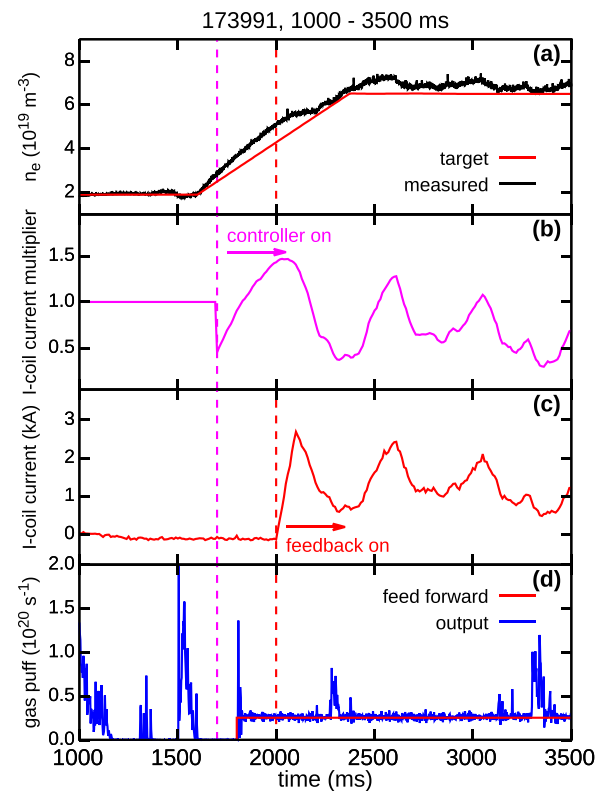

Figure 10. Demonstration of density feedback control using gas puff and 3D fields as actuators: (*a*) n_e, (*b*) coil current multiplier, (*c*) MP coil current, (*d*) gas puff. When the sensor n_e is above the n_e target the 3D field amplitude is increased to reduce n_e, whereas as additional gas is injected when n_e tends to fall below the target n_e.

undershoots of the density target. This leads to gas injection already before the density becomes smaller as the target. The maximum gas puff introduced by this offset is set to be smaller than the feed-forward gas puff component. This strategy is sometimes used to avoid undershoots of the density target, avoiding optimization of the gas controller gains. Therefore, additional gas is already introduced when the MP coils are not fully down to their minimum amplitude. The minimum MP coil amplitude is set by the simultaneously running standard EFC controller. In the presented case, the EFC controller uses the same set of MP coils as the pedestal n_e controller.
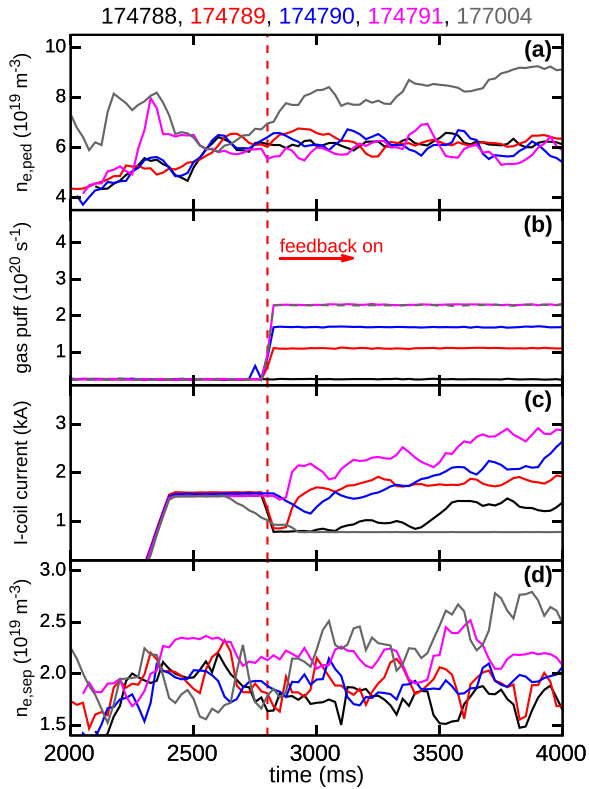
Figure 11. Demonstration of 3D field density feedback for varied feed-forward gas puff: (*a*) pedestal top electron density ($n_{e,ped}$), (*b*) gas puff, (*c*) MP coil current and (*d*) separatrix electron density ($n_{e,sep}$). As the gas is increased from discharge to discharge, the MP coil current is feedback controlled such that a constant $n_{e,ped}$ is achieved in comparison to an uncontrolled reference at maximum gas puff (gray).

This simple control scheme is so far mostly operated under conditions when the density target is set below the 'natural' plasma density. Therefore, the MP coils are the dominantly used actuators. There is headroom for controller optimization in the sense that the gains and controller timescales can be adapted such that controller oscillations are smoothed out. The plasma response to gas puff and 3D fields is strongly dependent on the selected plasma scenario, which requires adaption of controller gains if the target scenario is changed. Nevertheless, the presented plasma discharge demonstrates a proof of principle for a multi-actuator n_e controller. The combination of 3D fields and gas puff allows to adjust the n_e in both directions and achieve the requested n_e target. Moreover, the MP coils enable a faster timescale of density control since they are causing a faster response of the n_e than gas puffs.

4.3. Controlling the density pedestal in Super H-mode experiments

To couple reactor relevant divertor conditions to Super H-mode, the collisionality in the divertor region has to be raised by introducing additional gas to the divertor plasma. This eventually leaks to the confined plasma region, leading to an unfavorable density increase. Correspondingly, the pedestal collisionality decreases going in hand with a performance
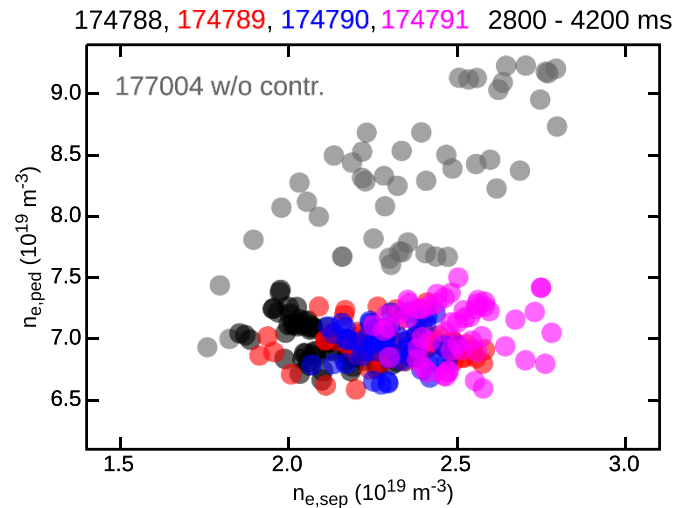

Figure 12. Decoupling of $n_{e,sep}$ and $n_{e,ped}$: $n_{e,ped}$ is kept constant by pedestal n_e feedback control, therefore, only $n_{e,sep}$ is affected as gas is introduced. This decouples the 'natural' $n_{e,sep}$ and $n_{e,ped}$ evolution without activated controller (gray).

reduction. As a task of core-edge optimization the unfavorable pedestal density increase can be counteracted by application of the introduced pedestal density feedback control. Figure 11 shows the capabilities of regulating the pedestal top electron density ($n_{e,ped}$) using 3D fields, during a discharge-by-discharge gas puff variation.

As additional gas is introduced to the plasma (figure 11(*a*)), the $n_{e,ped}$ feedback control is turned on to regulate the MP coil current (figure 11(*c*)). While the $n_{e,ped}$ remains roughly constant throughout the discharges, the average MP coil current increases as the feed-forward gas puff rate is stepped up. A reference shot (gray) shows the evolution of $n_{e,ped}$, when the density control is inactive. Here, the MP coil is set feed-forward to the lower boundary of the allowed control range and the highest gas puff rate of the scan is applied. As the gas is injected, $n_{e,ped}$ as well as $n_{e,sep}$ continuously rise towards the end of the discharge.

Within the feed forward gas puff scan, $n_{e,sep}$ is varied by roughly 25% as shown in figure 12. A similar variation of $n_{e,sep}$ is also seen in the reference discharge (gray) with inactive pedestal n_e feedback controller. However, this leads to an unwanted, significant increase of $n_{e,ped}$ away from the desired density target of Super H-mode. With activated pedestal n_e feedback control, $n_{e,ped}$ can be decoupled from $n_{e,sep}$ and kept close to desired target. This allows to maintain favorable low collisionality pedestal top conditions, while moving towards plasma conditions at the separatrix that allow for efficient power exhaust. The presented application of pedestal control highlights that pedestal control schemes can support physics experiments targeting plasma performance optimization.

5. Prospects towards ITER control

In next step fusion devices such as ITER, advanced control techniques will become more important since performance

needs to be maximized while staying within operational limits as well as physics boundaries. Examples are force limits that restrict the maximal applicable coil current ramp rates and the physics parameter space of e.g. sustainable ELM suppression. Nuclear operation of ITER will be different than control of present-day machines [53]. Although some control aspects are already covered in present-day tokamaks, the requirements on ITER's PCS are multifaceted and require input of multiple RT diagnostics [54, 55]. Furthermore, every algorithm needs to be qualified and tested before being executed during plasma discharges, which requires a suitable control simulation platform [56] and a step wise implementation [57]. For the first plasma, only a reduced set of actuators as well as control algorithms are required [58]. Further PCS development will be performed in stages as moving towards nuclear operation [59]. Within this process more operational limits will be approached, which will require appropriate control tools to ensure safe machine operation. This includes control schemes for reliable disruption avoidance and mitigation [60], full RT wall load monitoring [61, 62], divertor radiated power control [63, 64] or burn control [65].

Owing to the high pedestal pressure and consequently the intolerable ELM energy losses on the walls, ELM control is a necessity to protect the ITER divertor. To avoid tungsten (W) accumulation, f_{ELM} control schemes were implemented and routinely used at JET [66]. As this machine moves towards its next deuterium-tritium (D-T) campaign, a number of control schemes are required [67], that allow for safe machine operation and optimal usage of the available neutron budget [68]. For ITER D-T operation, reliable ELM control is one of the biggest challenges. Therefore, it is equipped with various, well suited actuators including 27 individually powered MP coils, a variety of gas valves and pellet injectors [14, 15]. MP ELM suppression is one of the main strategies to avoid ELMs and for this reason it is important to demonstrate the sustainment of such conditions in long plasma discharges as ITER will have. Recent experiments at KSTAR achieved MP ELM suppression for more than 30 s [19], however, the plasma and first-wall conditions still evolve on these longer timescales and towards the end of the discharge ELM suppression is lost. This emphasizes the necessity of actively controlling the MP coils during long pulse operation to ensure an optimal configuration of the fields at any time of the plasma discharge. Especially, when e.g. wall conditions are evolving on a multi-second timescale, pre-programmed feed-forward control becomes unfeasible and a RT decision process is required. Before being implemented for ITER, all advanced control schemes need to demonstrate their feasibility, at least as a proof of principle, in present-day machines. The pedestal control development at DIII-D evolves this effort towards including 3D field edge density control and optimized MP ELM suppression. To avoid the hysteresis effect of the MP on confinement, ITER would need to have an adaptive ELM control algorithm that keeps the MP amplitude as low as necessary to sustain ELM suppression. The initial DIII-D experiments described here have shown that pedestal and ELM control schemes can enable high performance ELM-free operations. Such schemes can be evolved to higher sophistication and deployed to ITER in

the future. An ELM control system could dynamically adjust the MP perturbation structure based on the modeled plasma response and optimize for ELM suppression, while regulating the degree of optimal suppression without excessive confinement degradation. Optimization of MP amplitudes to the minimum needed for ELM suppression allows improved global confinement, otherwise there is the risk of locking in reduced plasma performance. This is especially important for achieving high fusion energy gain factor (Q), since $H_{98(y,2)}$ enters to the power of 3.23 in Q [69]. Further control development and multi-machine comparisons are needed to achieve the goal of reliable ELM-free operation at maximum Q for ITER.

6. Summary

Three control schemes using non-axisymmetric 3D magnetic fields as actuators were implemented and tested at DIII-D. The first one allows for optimization of ELM-suppressed plasmas in terms of controlling the 3D field amplitude at the transition into MP ELM suppression reducing the hysteresis of plasma confinement. The second control method aims towards re-fueling the density 'pump-out' by injection of additional gas, enabling studies of the transition into and out of MP ELM suppression at constant density. Here, a limit cycle behavior of edge rotation and MP amplitude persists. A third density feedback controller uses MP fields and the associated density 'pump-out' to regulate the pedestal n_e, providing controlled conditions for physics experiments. The utilization of this controller allows to loosen the tight coupling of separatrix and pedestal top density. This enables the investigation of integrated core-edge scenarios with high performance pedestals and a radiative divertor.

7. Outlook towards integrated ELM control

Advanced control schemes are a necessity moving forward towards new fusion devices. Fully feed-forward, pre-programmed discharges could lead to severe machine damage, e.g. when ELM suppression is lost due to changing machine conditions. For this reason, RT algorithms and decision-making based on RT measurements are required to ensure safe machine operation at any time and to optimize plasma performance.

Present-day devices as DIII-D provide an excellent test bed for developing new advanced control strategies. With respect to MP ELM suppression control it is envisaged to couple the implemented RT response model with an MP coil amplitude and phase optimization. The minimum required 3D fields could be applied to transition into and to sustain ELM suppression at any time without degrading confinement more than necessary. Semi-empirical models will need to be utilized to determine the ELM suppression threshold until a first principle understanding of MP ELM suppression is established. It is likely required to expand the control strategy towards adaptive control schemes when the controller is active during transient events as I_p ramps and L-H transitions.

In conclusion, active control schemes will enable safe operation at maximized gain in future devices as ITER. Their implementation in present-day machines provides proofs of principle and guides their future development. Moreover, by means of control, integrated, reactor relevant plasma scenarios can be accessed in current devices, enabling their detailed study.

7. Acknowledgment

Disclaimer

ORCID iDs

F.M. Laggner https://orcid.org/0000-0003-1601-2973
D. Eldon https://orcid.org/0000-0003-1895-0648
A.O. Nelson https://orcid.org/0000-0002-9612-1936
C. Paz-Soldan https://orcid.org/0000-0001-5069-4934
A. Bortolon https://orcid.org/0000-0002-0094-0209
T.E. Evans https://orcid.org/0000-0002-8357-5859
B.A. Grierson https://orcid.org/0000-0001-5918-6506
Q. Hu https://orcid.org/0000-0002-8877-4988
D.A. Humphreys https://orcid.org/0000-0002-0879-4074
R. Nazikian https://orcid.org/0000-0001-6235-6692
O. Meneghini https://orcid.org/0000-0001-5100-5483
P.B. Snyder https://orcid.org/0000-0002-0613-4232
E.A. Unterberg https://orcid.org/0000-0003-1353-8865
E. Kolemen https://orcid.org/0000-0003-4212-3247

References

[1] Leonard A.W. 2014 *Phys. Plasmas* **21** 090501
[2] Loarte A. *et al* 2003 *Plasma Phys. Control. Fusion* **45** 1549–69
[3] Lang P.T. *et al* 2013 *Nucl. Fusion* **53** 073010
[4] Loarte A. *et al* 2014 *Nucl. Fusion* **54** 033007
[5] Evans T.E. *et al* 2004 *Phys. Rev. Lett.* **92** 235003
[6] Jeon Y.M. *et al* 2012 *Phys. Rev. Lett.* **109** 035004
[7] Sun Y. *et al* 2016 *Phys. Rev. Lett.* **117** 115001
[8] Suttrop W. *et al* 2017 *Plasma Phys. Control. Fusion* **59** 32–46
[9] Fenstermacher M.E. *et al* 2008 *Phys. Plasmas* **15** 056122
[10] Wade M.R. *et al* 2015 *Nucl. Fusion* **55** 023002
[11] In Y. *et al* 2017 *Nucl. Fusion* **57** 116054
[12] Paz-Soldan C. *et al* 2019 *Nucl. Fusion* **59** 056012
[13] Schaffer M.J. *et al* 2008 *Nucl. Fusion* **48** 024004
[14] Neumeyer C. *et al* 2011 *Fusion Sci. Technol.* **60** 95–9
[15] Daly E.F. *et al* 2013 *Fusion Sci. Technol.* **64** 168–75
[16] Unterberg E.A. *et al* 2010 *Nucl. Fusion* **50** 034011
[17] Paz-Soldan C. *et al* 2016 *Nucl. Fusion* **56** 056001
[18] Cui L. *et al* 2017 *Nucl. Fusion* **57** 116030
[19] Park H.K. *et al* 2019 *Nucl. Fusion* **59** 112020
[20] Solomon W.M. *et al* 2014 *Phys. Rev. Lett.* **113** 135001
[21] Solomon W.M. *et al* 2016 *Phys. Plasmas* **23** 056105
[22] Hughes J.W. *et al* 2018 *Nucl. Fusion* **58** 112003
[23] Snyder P.B. *et al* 2015 *Nucl. Fusion* **55** 083026
[24] Snyder P.B. *et al* 2019 *Nucl. Fusion* **59** 086017
[25] Humphreys D.A. *et al* 2007 *Nucl. Fusion* **47** 943–51
[26] Ferron J. *et al* 1991 An advanced plasma control system for the DIII-D tokamak *14th IEEE/NPSS Symp. Fusion Eng.* (San Diego, CA, 30 September- 3 October 1991) **2** 761–4
[27] Penaflor B.G. *et al* 2004 *Fusion Eng. Des.* **71** 47–52
[28] Carlstrom T.N., Ahlgren D.R. and Crosbie J. 1988 *Rev. Sci. Instrum.* **59** 1063–6
[29] Carlstrom T.N. *et al* 1992 *Rev. Sci. Instrum.* **63** 4901–6
[30] Eldon D. *et al* 2012 *Rev. Sci. Instrum.* **83** 10E343
[31] Groebner R.J. and Carlstrom T.N. 1998 *Plasma Phys. Control. Fusion* **40** 673–7
[32] Eldon D. *et al* 2017 *Nucl. Fusion* **57** 066039
[33] Chirikov B.V. 1979 *Phys. Rep.* **52** 263–379
[34] Park J.K. *et al* 2007 *Phys. Plasmas* **14** 052110
[35] Ryan D.A. *et al* 2017 *Plasma Phys. Control. Fusion* **59** 024005
[36] Park J.K. *et al* 2018 *Nat. Phys.* **14** 1223–8
[37] Scoville J.T. and Haye R.J.L. 2003 *Nucl. Fusion* **43** 250–7
[38] Paz-Soldan C. *et al* 2014 *Nucl. Fusion* **54** 073013
[39] Snyder P.B. *et al* 2002 *Phys. Plasmas* **9** 2037–43
[40] Snyder P.B. *et al* 2012 *Phys. Plasmas* **19** 056115
[41] Nazikian R. *et al* 2014 Advances in the understanding of ELM suppression by resonant magnetic perturbations (RMPs) in DIII-D and implications for ITER *Proc. 25th Int. Conf. on Fusion Energy* (St Petersburg, Russian Federation, 2014) EX/1-1 (http://www-naweb.iaea.org/napc/physics/FEC/FEC2014/fec2014-preprints/205_EX11.pdf)
[42] Lee J. *et al* 2019 *Nucl. Fusion* **59** 066033
[43] Mlynek A. *et al* 2011 *Nucl. Fusion* **51** 043002
[44] Janky F. *et al* 2015 *Fusion Eng. Des.* **96-97** 637–40
[45] Brunner K.J. *et al* 2018 *J. Instrum.* **13** P09002–P09002
[46] Blanken T.C., Felici F., Rapson C.J., de Baar M.R., Heemels W.P.M.H. the TCV team and the ASDEX-Upgrade team 2018 *Fusion Eng. Des.* **126** 87–103
[47] Felici F. *et al* 2018 *Nucl. Fusion* **58** 096006
[48] Zeeland M.A.V. *et al* 2013 *Rev. Sci. Instrum.* **84** 043501
[49] Imazawa R., Kawano Y., Itami K. and Kusama Y. 2014 *Conf. Proc.* **1612** 61–8
[50] Orsitto F.P. *et al* 2016 *Nucl. Fusion* **56** 026009
[51] Lang P.T. *et al* 2018 *Nucl. Fusion* **58** 036001

[52] Greenfield C.M. *et al* 1990 *Rev. Sci. Instrum.*
    61 3286–8
[53] Humphreys D. *et al* 2015 *Phys. Plasmas* **22** 021806
[54] Snipes J.A. *et al* 2010 *Fusion Eng. Des.* **85** 461–5
[55] Snipes J.A. *et al* 2012 *Fusion Eng. Des.* **87** 1900–6
[56] Winter A. *et al* 2015 *Fusion Eng. Des.* **96-97** 720–3
[57] Zabeo L. *et al* 2019 *Fusion Eng. Des.* **146** 1446–9
[58] Walker M.L. *et al* 2019 *Fusion Eng. Des.* **146** 1853–7
[59] de Vries P.C. *et al* 2018 *Fusion Eng. Des.*
    129 334–40
[60] Pautasso G. *et al* 2018 *Nucl. Fusion* **58** 036011

[61] Anand H. *et al* 2018 *Fusion Eng. Des.* **137** 143–51
[62] Anand H. *et al* 2020 *Nucl. Fusion* **60** 036011
[63] Guillemaut C. *et al* 2017 *Plasma Phys. Control. Fusion*
    59 045001
[64] Eldon D. *et al* 2019 *Nucl. Mater. Energy* **18** 285–90
[65] Hawryluk R.J. *et al* 2015 *Nucl. Fusion* **55** 053001
[66] Lennholm M. *et al* 2015 *Nucl. Fusion* **55** 063004
[67] Lennholm M. *et al* 2017 *Fusion Eng. Des.* **123** 535–40
[68] Piron L. *et al* 2019 *Fusion Eng. Des.* **146** 1364–8
[69] Zohm H. 2010 *Fusion Sci. Technol.* **58** 613–24
[70] Meneghini O. *et al* 2015 *Nucl. Fusion* **55** 083008